Supporting Information for

Single enzyme studies reveal the existence of discrete functional states for monomeric enzymes and how they are "selected" by allosteric interactions

Nikos S. Hatzakis[a,b,c,‡,*], Li Wei[a,b,c,‡], Sune K. Jorgensen[a,†1], Andreas H. Kunding[a,b,c], Pierre-Yves Bolinger[a,b,c,†2], Nicky Ehrlich[a,b,c], Ivan Makarov[a,b,c], Michael Skjot[d,†3], Allan Svendsen[d], Per Hedegård[e], Dimitrios Stamou[a,b,c,*]

[a]Bio-Nanotechnology Laboratory, Department of Neuroscience and Pharmacology, [b]Nano-Science Center, [c]Lundbeck Foundation Center Biomembranes in Nanomedicine, University of Copenhagen, 2100 Copenhagen, Denmark
[d]Novozymes A/S, Department of Protein Biochemistry, 2880 Bagsvaerd, Denmark
[e]Nano-Science Center, Niels Bohr Institute, University of Copenhagen, Denmark

Supporting Methods

All chemical were used as received, unless otherwise stated. Nanopure water was used for the preparation of all buffers.

Liposome preparation and surface immobilization

The liposomes were prepared as described earlier [1]. A typical preparation contained a ratio of 92.8/5/0.1 for 1,2-Dioleoyl-sn-Glycero-3-Phosphocholine (DOPC) (Avanti), 1,2-Dioleoyl-*sn*-Glycero-3-[Phospho-*rac*-(1-glycerol)] Sodium Salt (DOPG) (Avanti) and 1,2-distearoyl-sn-glycero-3-phosphoethanolamine-N-[biotinyl(polyethylene glycol)-2000] (ammonium salt) (DSPE-PEG_{2000}-biotin) (Avanti) respectively, 0.1 % of 1,1'-dioctadecyl-3,3,3',3'-tetramethyl-indodicarbocyanine perchlorate (DiD) (Invitrogen) and the desired amount of 1,2-dioleoyl - *sn*– glycerol – 3 – phosphoethanolamine – N - [methoxy (polyethylene glycol) -2000] (ammonium salt) (DOPE-PEG_{2000}) (Avanti). The liposomes were immobilized on glass surface passivated with BSA (Sigma) and Streptavidin (Sigma) according to a previously published protocol [1-3].

Enzyme expression and purification.

Variants of TLL and CALB were generated and purified as described previously [4,5]. The TLL variant employed has the following point mutations, K24R K46R G61C K74R K98R K127R D137K K223R K237R and contains one free Cys and one free Lys (see Figure S1A). The CALB variant employed has the following point mutation S28C (Figure S1B). The presence of a single anchoring point enables the directional immobilization on liposomes. The purity of both TLL and CALB is shown in the SDS PAGE gels in Figure S2.

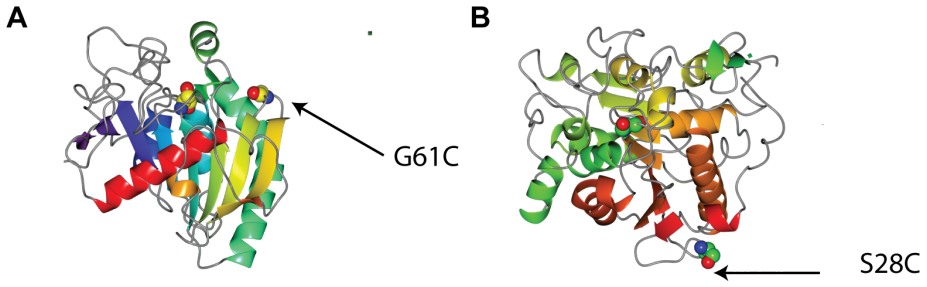

Figure S1. Position of solvent accessible cyst mutations for **A.** TLL and **B.** CALB. The point mutations and the active site serine are shown in space filling model in both cases. The figures are made by ccp4mg software using the pdb files of 1DT3 and 1TCB for TLL and CALB respectively.

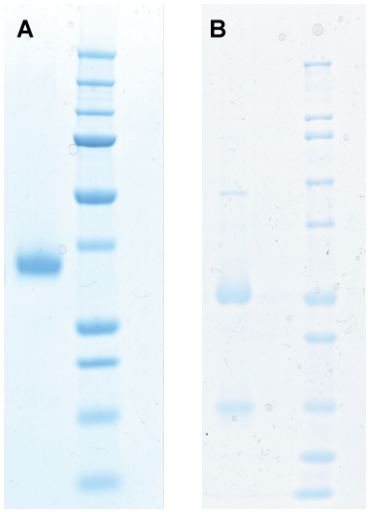

Figure S2. SDS electrophoresis chromatographs labeled with Comassie blue showing the purity of **A.** TLL and **B.** CALB constructs employed in this study.

Lipase –Streptavidin conjugation

Coupling of TLL and CALB with biotin was performed according to manufactures protocol after reduction of the solvent accessible cysteine by TCEP. In a typical experiment the reduction solution was prepared by mixing 10 µl of 872 mM TCEP with 14 µl of 2 mM NaOH. 0.5 µl of this reducing solution was added to 500 µl of 45 µM enzyme and allowed to react for ~ 10 min. Prior to thiol coupling the oxygen in the reaction mixture was removed by applying vacuum for 10 min and followed by purging argon. To this end 43 µl of 19 mM N-(3-maleimidylpropionyl) biocytin (Invitrogen) was added to the mixture and allowed to react for ~2h in room temperature. The biotinylated enzyme was purified from unreacted reagents using FPLC equipped with Superdex G200 or Superdex G75 size exclusion column. The purified enzyme was allowed to react with a 2.5 fold excess of 488 labeled Streptavidin (Invitrogen) to ensure that only one lipase would be coupled to the labeled Streptavidin. The resulting conjugate was isolated from unreacted SAV^{488} by fractionation using FPLC, see Figure S3. Careful selection of fractions permitted us also to discard the small impurities present in the CALB preparation (Figure S2) and isolation of the pure CALB-SAV^{488} construct as shown in Figure S3B. The final buffer was 20 mM PBS buffer pH = 7.2.

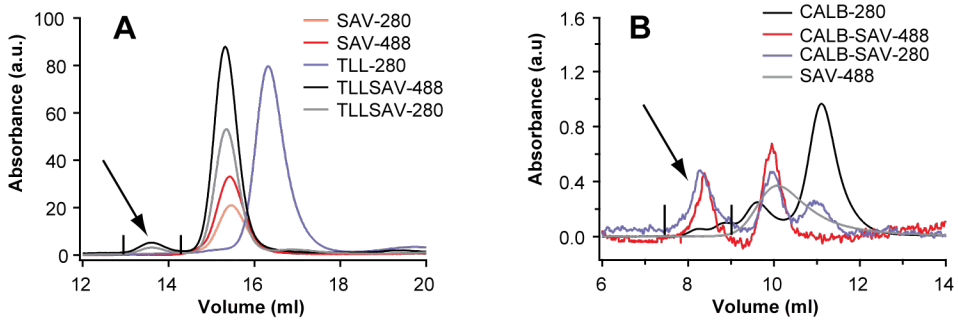

Figure S3. Purification of TLL-SAV^{488} and CALB-SAV^{488} conjugate using FPLC equipped with size exclusion column. **A.** Purification and isolation of the TLL-SAV^{488} was obtained by using a Superdex G200 size exclusion column. Careful selection of the fraction indicated by the arrow permitted isolation

of TLL-SAV^{488} from unreacted SAV. **B.** Purification and isolation of CALB-SAV^{488} was obtained by using a Superdex G75 size exclusion column and collection of the fraction indicated by the arrow. This methodology permitted isolation of the pure CALB-SAV^{488} construct from unreacted SAV and the small impurities present in the CALB preparation (also shown in the gel of Figure S2).

Single enzyme immobilization on liposomes

To limit non specific binding of enzymes on glass surface we incubated enzymes with liposomes in solution prior to immobilization on the surface. In a typical experiment we premixed 10 µl of 30 nM labeled TLL and 60 µl of 2 g/l of 50 nm extruded liposomes and incubated overnight. 20 µl of the mixture was added on the microscope surface and was incubated for ~ 10 min before washing. Using these concentration resulted in only ~ 5 % of liposomes having bound enzymes thus making it statistically unlikely for a liposome to contain a second enzyme ($P < 0.12$ %).

To further prove that the majority of vesicles contained one enzyme we plotted the intensity distribution of the alexa fluor 488 labeled conjugates that are bound on vesicles. Please note that only the streptavidin molecules are coupled with Alexa fluor 488. As shown in Figure S4 a single population of species is observed justifying the presence of single enzymes on vesicles. The fact that each streptavidin has on average 4 fluorescent labels would be default introduce a large spread in the intensity histogram. Therefore in Figure S4 we compared the experimental intensity distribution of the data (green bars) to the calculated poisson distribution of intensities for 1, 2 and 3 enzymes (black, red and blue line respectively) having on the average 4 alexa labels. As can be clearly seen in Figure S4 the majority of loaded vesicles contain one enzyme in agreement with the statistical analysis.

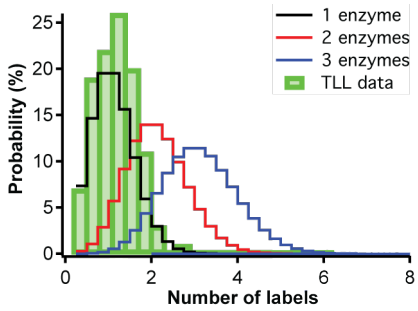

Figure S4. Intensity Distribution of alexa-fluor488 labeled enzymes bound on vesicles. Green bars correspond to the experimental distribution of intensities collected from 1000 vesicles, 50 of which had enzymes bound, Data are normalized to 1. A single population of species is observed. The black red and blue lines correspond to the normalized simulated poissonian distributions of intensities for 1, 2, and 3 enzyme respectively having 4 alexa fluor 488 labels per enzyme. The data clearly illustrate that the majority of bound vesicles contain one enzyme

Fluorescent Measurements

Confocal Laser microscopy

All samples were examined with a Leica TCS SP5 inverted confocal microscope using an oil immersion objective HCX PL APO CS × 100 (NA 1.46) and equipped with two Avalanche Photodiode Detectors (APDs). Substrate detection was obtained by a 20 MW 488 laser line and vesicle detection by a 633 laser line. Signal splitting was accomplished using a 560 nm beam splitter, detection of protein and enzymatic turnovers was measured through an ET 525/25 filter

and liposome detection through a HQ 670/55 filter. The temperature was monitored in the room and the microscope and remained constant at 22 ± 1°C.

Threshold setting for enzymatic activity traces.

The histogram in Figure 1d is composed of a background distribution and a signal distribution. To distinguish background from enzymatic activity traces a threshold level has to be set. Above the threshold value a fluorescent spike is considered as an enzymatic turnover and below that as background. To correctly identify the background distribution we obtained background trace by measuring fluorescent intensity on an empty vesicle located next to the active enzyme and fitted it with a Poisson. To insure that the background measured was identical with the background in the activity trace and not biased by the autohydrolysis of CFDA we acquired data directly after the activity trace acquisition. Next we fitted the histogram of the intensity time trace (Figure 1d and zoomed in region in Figure S5) with two Poisson distributions using the fits of the independent background trace as guesses for the background distribution. The intersection of the two yielded Poisson distributions yields the threshold above which a fluorescent burst is considered as an enzymatic turnover. Under our experimental conditions the false positives from bg contribution are 10-20% depending on the PEG concentration. As discussed in section "Intensity fluctuations" in page 17 these false positive events do not in any measurable way bias our findings"

CFDA can be autohydrolyzed to FAM under our experimental conditions resulting in a continuous slow background signal increase. To avoid significant background built up that could limit the accuracy of our experiments each experiment is performed for a maximum of 30 min. After that a new sample with freshly prepared CFDA was used.

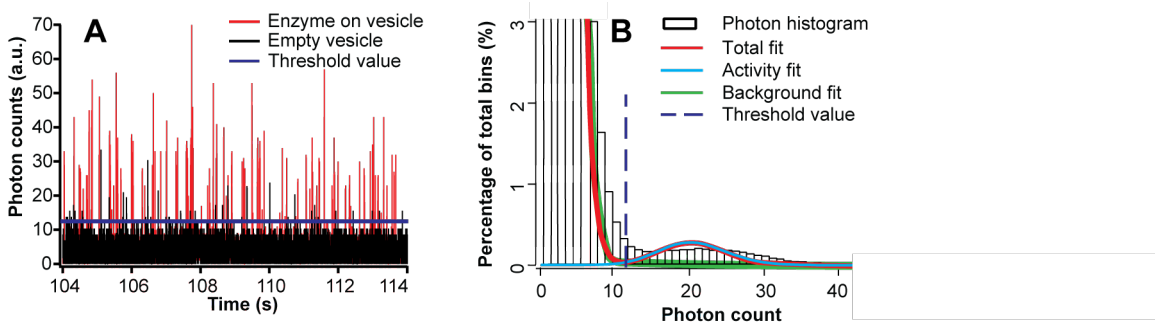

Figure S5. A. 10 sec zoomed in region of the time trace shown in Figure 1D. Red line corresponds to the intensity trace of an active enzyme located on vesicle. Black line corresponds to the background signal as collected on a vesicle without enzyme located close to the enzyme containing one. Dark blue line corresponds to the threshold value used **B.** intensity histogram of the enzymatic trajectory of A. Histogram was fitted with a double poisson distribution (red line), one corresponding to background (green line) and one to the enzymatic activity trace (blue line). The intersection of the two poissonian distributions was used to set the threshold (dashed dark blue line).

Fluorescent spectrometer

Fluorescent measurements in bulk were carried out on a Horiba Jobin Yvon FluoroMax-4 spectrofluorometer at room temperature with quartz cuvettes of 1 or 0.3 cm path length and using excitation emission wavelengths of 488 and 525 respectively.

Control Experiments

Single molecule kinetics is measured at saturating conditions.

The two activity state model developed in this manuscript describes enzymatic behavior at saturating conditions where substrate diffusion in the active site is not rate limiting. To insure that all measurements were performed at saturating CFDA concentrations we quantified the Michaelis-Menten kinetics for both TLL and CALB on CFDA using ensemble measurements (see Figure S6). For TLL we found $K_M = 32.2 \pm 4.0$ μM and a $V_{max} = 7.8 \pm 0.9$ nM min^{-1}. Data are obtained for 100 nM of TLL variant. For CALB we found $K_M = 11.2 \pm 1.1$ μM and a $V_{max} = 6.32 \pm 0.2$ nM min^{-1}. The corresponding specific activity of 0.8 ± 0.05 nmole min^{-1} mg^{-1} is in good agreement with earlier studies[6]. Data are obtained for 200nM of CALB variant. To insure that single molecule kinetics were monitored at saturating substrate concentrations all experiments were performed at 100 μM CFDA.

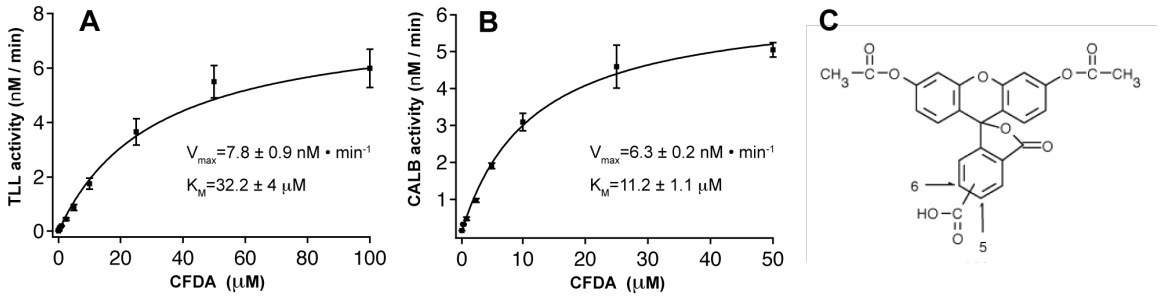

Figure S6. Quantification of Michaelis-Menten constants of TLL and CALB for CFDA hydrolysis **A)** For TLL a $K_M = 11.2 \pm 1.1$ μM and a $V_{max} = 6.32 \pm 0.2$ nM min^{-1} was measured. The corresponding specific activity of 0.8 ± 0.05 nmole min^{-1} mg^{-1} is in good agreement with earlier studies [6]. Data are obtained for 200 nM of CALB variant. **B)** For CALB a $K_M = 32.2 \pm 4.0$μM and a $V_{max} = 7.8 \pm 0.9$ nM min^{-1} was measured. Data are obtained for 100 nM of TLL variant. Single molecule experiments were performed at 100 μM CFDA to insure saturating conditions. Experiments were performed on a Horiba Jobin Yvon FluoroMax-4 spectrofluorometer using a 50 μl cuvette exciting at 488 nm (excitation slit 3) and detecting at 525 nm (emission slit 15). The error bars correspond to standard deviation of two independent experiments. **C**) Structure of prefluorescent substrate CFDA

Enzymatic product carboxyfluorescein (FAM) is not absorbed on liposomes

To insure that product (FAM) is not absorbed on liposomes we performed two types of control experiments. During experimental acquisition we focused the laser beam on an empty liposome and recorded the time trace. As showed in Figure 1d we cannot detect any product being absorbed on liposomes at 100 μM CFDA concentrations. To insure that the absence of measurable signal is not due to diminished product concentration under the experimental conditions we chemically hydrolyzed substrate 5-(and-6)-carboxy-fluorescein diacetate (CFDA) to FAM and quantified its diffusion time by FCS. Using 1 nM FAM we compared the diffusion time of FAM in solution and in the presence of liposome. As shown in Figure S7 in both cases we obtained identical diffusion coefficient $D = 423 \pm 24$ μm s^{-1} and a triplet state time $6.8 \times 10^{-7} \pm 2.12 \times 10^{-7}$ in good agreement with earlier studies [7].

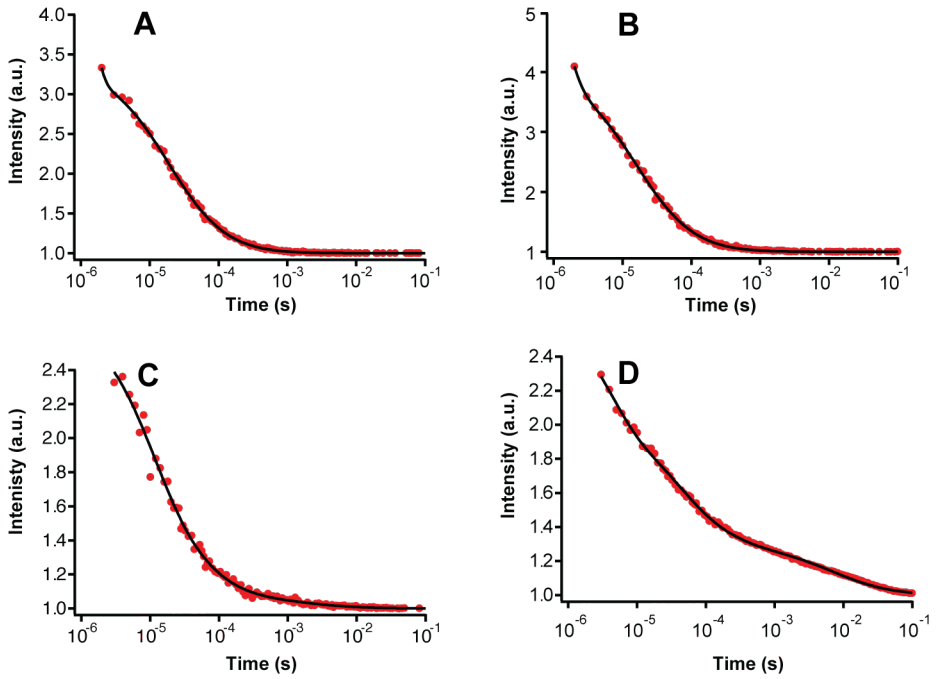

Figure S7. Fluorescent Correlation Spectroscopy (FCS) measurements showing that the single molecule measurements are not biased by product release from enzyme or product accumulation on vesicles. **A.** FCS trace of FAM in solution, away from any liposome or enzyme, at 1 nM concentration. A single diffusion particle was found with a diffusion time of 423 ± 24 $\mu m^2 s^{-1}$ and a triplet state time $6.8\times10^{-7} \pm 2.12\times10^{-7}$ in good agreement with earlier reported values [7]. **B.** FCS trace obtained on a surface immobilized vesicle without lipase at 1 nM of FAM concentration. In full agreement with the data in solution a single diffusion particle was found with a diffusion coefficient of 423 ± 24 $\mu m^2 s^{-1}$ and a triplet state time of $6.8\times10^{-7} \pm 2.12\times10^{-7}$ s^{-1}. Thus no measureable product accumulation on vesicles is observed. **C.** FCS of product formation from an active TLL immobilized on a vesicle. The product FAM was found to spend 1.8 ± 0.3 ms in the enzyme before it diffuses away. **D.** FCS of product formation from a vesicle immobilized active CALB. The product FAM was found to spend 2.2 ± 0.5 ms in the enzyme before it diffuses away. Data in A, B are fitted for single diffusing particle. Data in C,D are fitted for particles with two different diffusing coefficients using the triplet state time and diffusion coefficients of the fast particle extracted from the fits in A and B [8].

Product release is not rate limiting and is not the cause of dynamic disorder.

To insure that product FAM release from enzyme is not the rate-limiting step in the enzymatic cycle we measured its diffusion from the enzyme active site by FCS spectroscopy. In a typical experiments the laser beam was parked on a vesicle immobilized enzyme at saturating CFDA concentrations. We fitted the FCS curve for two diffusing particles having a triplet state. The diffusion coefficient and triplet state time used was obtained from FCS measurements in solution (Figure S7A). We found that product molecules after being formed they spend on average 1.8 ± 0.3 ms and 2.2 ± 0.5 ms for TLL and CALB respectively in the confocal volume before they diffuses away (See Figure S7C and Figure S7D respectively). Since one turnover cycle occurs every 40 ms and 30 ms on average for TLL and CALB respectively we can safely conclude that product release is not rate limiting.

To examine if product release contributes to dynamic disorder we plotted the distribution of on times. As shown in Figure S8 we obtained monoexponential decay for both TLL and CALB illustrating the product after being formed it diffuses away from the active site following a single

rate. Therefore the dynamic disorder in the reaction rate is not an artifact originating from the time FAM spends in the enzyme.

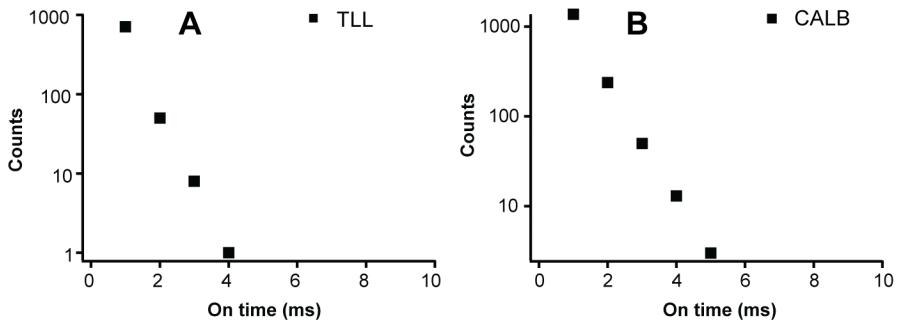

Figure S8. Distribution of the time the product remains in the enzymes active site before it is released in solution for **A**.TLL and **B**.CALB. In both cases a monoexponential distribution is observed. There is not dynamic disorder in product release form enzyme's active site.

Product FAM is not blinking in the time scale of single molecule kinetics

We next examined if FAM blinking is biasing the measured kinetics measurements. To do this we immobilized single Biotin-Fluorescein (Piercenet) molecules on a Streptavidin surface and monitored their blinking behavior in experimental conditions otherwise identical to the ones used for measuring enzymatic activity. As shown in Figure S9 fluorescein's rate of intersystem crossing to the triplet state rate is $50 \pm 7s^{-1}$ in good agreement with earlier studies [9]. Since the product is released from the enzyme 10 times faster (~2 ms) FAM blinking is not in any way biasing the measured kinetics.

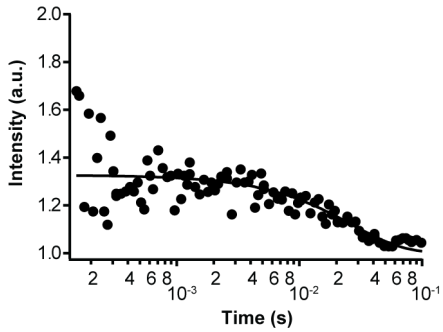

Figure S9. Blinking behavior of surface immobilized Fluorescein-biotin. Fluorescein blinking rate is $50 \pm 7s^{-1}$. Since product diffusion away from enzymes active site occurs in < 2 ms fluorescein blinking due to intersystem crossing is not biasing in any way the enzyme kinetics data.

Effect of liposomes on enzymatic activity of TLL and CALB.

Liposomes constitute a biocompatible 3D scaffold that spatially confines enzymes and in addition and significantly restricts non-specific interactions with the underlying solid surface and thus minimize surface introduced heterogeneities in the enzyme activity. Nevertheless the enzyme could statistically collide with the surface while sampling the surface of the liposome. To minimize this probability surface was passivated with streptavidin and BSA (pI = 6.5 and pI = 4.7

respectively)[10,11] that are both negatively charged at pH = 7.4. Since TLL is also negatively charged at this pH (pI = 5.1) it is repelled from the surface thus interactions with the surface is diminished.

To test the regulatory effect of liposomes on TLL activity we performed experiments in bulk. In a typical experiment we titrated 300 nM TLL with unlabeled liposomes extruded at 100 nm and measured its activity on 100 μM CFDA as a function of lipid concentration. We found that indeed activity of TLL is regulated in the presence of liposomes under our experimental conditions (see Figure S10A). Enzymes were found to have some residual activity in solution, which increase ~ 4 fold when titrating with liposomes in excellent agreement with the single molecule data of Figure 3. Fitting of the binding curve with Langmuir isotherms allowed us to calculate the enzyme-liposome dissociation constant. We found $k_d = 0.15 \pm 0.01$mM in agreement with earlier reported values measured on different lipid systems [12].

To insure that CALB activity is not affected by the presence of liposomes we measured the enzymatic activity in bulk at increasing liposome concentration. Titration of 100 nM of CALB with liposomes did not confer any measurable difference in the enzymatic activity towards CFDA as shown in as shown in Figure S10B. Liposomes therefore can be employed to confine single enzyme and monitor their catalytic behavior.

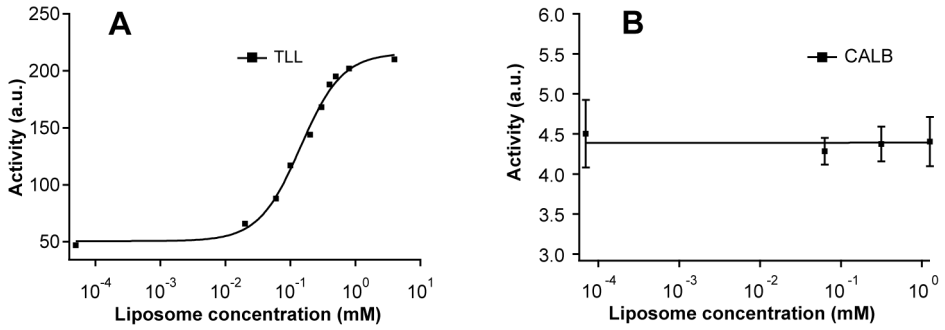

Figure S10. Effect of liposomes on the activity of the enzyme mutants. **A.** TLL as expected shows a strong increase in activity upon liposome addition. Increasing the liposome concentration resulted in 4 fold increase of TLL activity in good agreement with single molecule experiments in Figure 3. Fitting of the binding curve with Langmuir isotherm permitted us to calculate the dissociation constant k_d. The obtained value $k_d = 0.15 \pm 0.01$ mM is in good agreement with earlier reported values [13]. **B.** CALB shows no measurable activity variation in the presence of liposomes. The experiment was performed for 100 nM CALB. Error bars represent the standard deviation of 2 independent experiments.

Effect of PEG and PEGylated liposome on TLL activity

To insure that the results of Figure 3 are not an artifact of interactions of TLL with PEG we measured the enzymatic activity in bulk at increasing PEG concentrations. In a typical experiment we measured the activity of 400 nM TLL prior and after the addition of 10 mg / ml PEG-2000. As shown in Figure S11 no measurable variation of TLL activity is observed when compared to the enzyme in solution.

Incubation with 0.1 mg / ml liposomes containing the highest PEG concentration employed in the experiments (2.1 % molar) does not influence enzymatic activity on CFDA in any measurable way. The reduced activity therefore in the presence of PEGylated liposomes in Figure 3 is not an artifact of PEG interactions and originates from restricting enzyme's access to the bilayer.

To insure that measurements of identical activity in Figure S11 are not due to non enzymatic hydrolysis of CFDA we measured its autohydrolysis rate in otherwise identical conditions but in the absence of enzyme. We found autohydrolysis of CFDA to be negligible under these experimental conditions. The activity therefore of the lipase in solution is identical to the activity in the presence of PEGylated liposomes and the reduced activity in the presence of PEG on Figure 3 is due to sterically hindering the enzyme from accessing the bilayer.

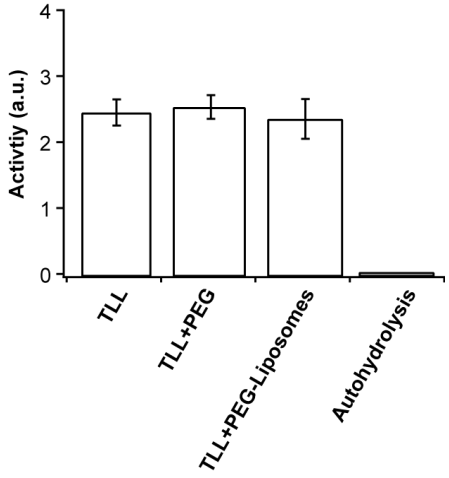

Figure S11. Influence of PEG and PEG-liposomes on TLL activity. Addition of 10 mg / ml PEG-2000 does not influence TLL activity in any measurable manner illustrating that the decreased activity in figure 3 is due to restricted TLL accessibility to the bilayer. The fact that the addition of 0.1 mg / ml liposomes containing 2.1 % PEG does not influence TLL activity illustrates that under these PEG concentrations TLL cannot access the bilayer. The rate of CFDA authydrolysis is shown for comparison. All measurements were performed on a sample containing 0.4 μM TLL.

Supporting text

Description of model with two activity states

Consider the model shown in the figure. A system can switch between two states, A_1 and A_2. In each of these states a reaction can take place, switching the system to one of the two states B_1 and B_2. We shall further assume, that the system will very quickly (i.e.. faster than any other time scale in the problem) return to either state A_1 or A_2, depending on which B state it reacted to.

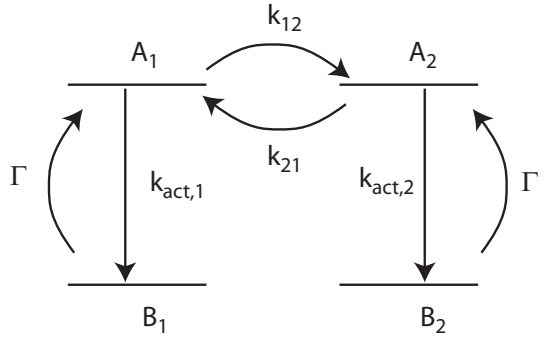

Figure S12. Two states with different activities.

In order to analyze the model, we shall introduce a number of useful propositions:

A_{it}**:** The system is in state A_i at time t

B_{it}**:** The system is in state B_i at time t

R_{it}**:** A reaction in state A_i takes place at time t

From this we can generate compound propositions like (using the notation: $A+B$ is "*A or B*" and AB is "*A and B*")

$R_t = R_{1t} + R_{2t}$**:** A reaction takes place at time t

$A_t = A_{1t} + A_{2t}$**:** The system is in either state A_1 or state A_2 at time t

$R_{it\Delta t} = B_{it+\Delta t}A_{it}$**:** A reaction takes place in state A_i in the time interval between t and $t+\Delta t$

$R_{t\Delta t} = R_{1t\Delta t} + R_{2t\Delta t}$**:** A reaction takes place in the time interval between t and $t+\Delta t$

$A_{1t+\Delta t}A_{2t}$**:** The system moves from state A_2 to state A_1 in the time interval between t and $t+\Delta t$

The reaction rates shown in the figure are defined by the following probabilities:

$$\begin{aligned} P(A_{2t+\Delta t}|A_{1t}I) &= k_{12}\Delta t \\ P(A_{1t+\Delta t}|A_{2t}I) &= k_{21}\Delta t \\ P(B_{1t+\Delta t}|A_{1t}I) &= k_{act,1}\Delta t \\ P(B_{2t+\Delta t}|A_{2t}I) &= k_{act,2}\Delta t. \end{aligned}$$

Here Δt is an infinitesimal time interval. I denotes background information, and $P(A|B)$ is the conditional probability of A *given* B.

We will be interested in the waiting time between two consecutive reactions. The probability density, $p_w(t)$, for this time is given by

$$p_w(t)\Delta t = P(R_{t\Delta t}|R_{0\Delta t}I).$$

It is implicitly understood in this probability, that *no* reaction is taking place in the time interval between 0 and t. By using the above relations and the basic rules of probability theory we can rewrite this quantity:

$$\begin{aligned} P(R_{t\Delta t}|R_{0\Delta t}I) &= \sum_i P(B_{it+\Delta t}A_{it}|R_{0\Delta t}I) \\ &= \sum_i P(B_{it+\Delta t}|A_{it}R_{0\Delta t}I)P(A_{it}|R_{0\Delta t}I) \\ &= \Delta t \sum_i k_{act,i}P(A_{it}|R_{0\Delta t}I) \end{aligned} \quad (1)$$

Similarly, the last factor can be rewritten by two applications of Bayes' rule

$$\begin{aligned} P(A_{it}|R_{0\Delta t}I) &= \frac{P(R_{0\Delta t}|A_{it}I)P(A_{it}|I)}{P(R_{0\Delta t}|I)} \\ &= \sum_j \frac{P(R_{j0\Delta t}|A_{it}I)P(A_{it}|I)}{P(R_{0\Delta t}|I} \\ &= \sum_j \frac{k_{act,j}P(A_{j0}|A_{it}I)P(A_{it}|I)}{\sum_l k_{act,l}P(A_{l0}|I)} \\ &= \sum_j P(A_{it}|A_{j0}I)w_j, \end{aligned} \quad (2)$$

where the weight factor, w_j is given by

$$w_j = \frac{k_{act,j} P(A_{j0}|I)}{\sum_l k_{act,l} P(A_{l0}|I)}. \tag{3}$$

The probabilities $p_{ij} = P(A_{it}|A_{j0}I)$ satisfy the equations

$$\begin{aligned} \frac{dp_{1j}}{dt} &= -(k_{act,1} + k_{12})p_1 + k_{21}p_2 \\ \frac{dp_{2j}}{dt} &= k_{12}p_1 - (k_{act,2} + k_{21})p_2. \end{aligned} \tag{4}$$

Note, that the return processes with rates Γ are not contributing the equations. This is to make sure that no reactions takes place in the interval between 0 and t. Setting Γ equal to zero will have the consequence, that 'histories' where a sojourn of the system to one of the B-states will not contribute to the probabilities in question.

The situation is different for the probabilities $P(A_{i0}|I)$ entering the weight factors. They can be evaluated by solving the equations satisfied by $P(A_{it}|I)$, namely

$$\begin{aligned} \frac{dP(A_{1t}|I)}{dt} &= -k_{12}P(A_{1t}|I) + k_{21}P(A_{2t}|I) \\ \frac{dP(A_{2t}|I)}{dt} &= -k_{21}P(A_{2t}|I) + k_{12}P(A_{1t}|I). \end{aligned} \tag{5}$$

Here even the reactions has been ignored altogether. This is because the return-rates, Γ, are assumed to be so large, that immediately after a reaction (with rate $k_{act,j}$) taking place in state A_j, the system will return to A_j, and we may as well ignore the reaction, when it comes to finding the probability of finding the system in state A_j. The background information I, does not include any information of what has happened in the system prior to time zero, hence $P(A_{j0}|I)$ is independent of this particular moment in time ($t = 0$). Therefore we conclude, that $P(A_{j0}|I)$ is obtained by setting the left hand sides of equal to zero and arrive at

$$P(A_{10}|I) = \frac{k_{21}}{k_{12} + k_{21}}, \qquad P(A_{20}|I) = \frac{k_{12}}{k_{12} + k_{21}}. \tag{6}$$

With this we can find the weights

$$w_1 = \frac{k_{act,1}k_{21}}{k_{act,1}k_{21} + k_{act,2}k_{12}}, \qquad w_2 = \frac{k_{act,2}k_{12}}{k_{act,1}k_{21} + k_{act,2}k_{12}}. \tag{7}$$

Returning to the probabilities $p_{ij}(t)$. They satisfy the equations (4), and the initial conditions $p_{ij}(0)=\delta_{ij}$. If we organize $p_{ij}(t)$ in a 2×2 matrix, the solution which is found by standard methods can be written

$$p_{ij}(t)=\mathbf{p}_+ e^{-\lambda_+ t}+\mathbf{p}_- e^{-\lambda_- t}, \tag{8}$$

where

$$\mathbf{p}_+=\begin{pmatrix} \frac{1}{2}\left(1+\frac{\delta}{\gamma}\right) & -\frac{\eta}{2\rho\gamma} \\ -\frac{\eta\rho}{2\gamma} & \frac{1}{2}\left(1-\frac{\delta}{\gamma}\right) \end{pmatrix}, \qquad \mathbf{p}_-=\begin{pmatrix} \frac{1}{2}\left(1-\frac{\delta}{\gamma}\right) & \frac{\eta}{2\rho\gamma} \\ \frac{\eta\rho}{2\gamma} & \frac{1}{2}\left(1+\frac{\delta}{\gamma}\right) \end{pmatrix}. \tag{9}$$

Here we have introduced the following notation

$$\begin{aligned} \lambda_\pm &= \alpha\pm\gamma, \qquad \gamma=\sqrt{\delta^2+\eta^2}, \\ \alpha &= \frac{k_{act,1}+k_{12}+k_{act,2}+k_{21}}{2}, \qquad \delta=\frac{k_{act,1}+k_{12}-k_{act,2}-k_{21}}{2}, \\ \rho &= \sqrt{\frac{k_{12}}{k_{21}}}, \qquad \eta=\sqrt{k_{12}k_{21}}. \end{aligned} \tag{10}$$

We now have all ingredients, and can give the final expression for the waiting time distribution

$$p_w(t)=(k_{act,1},k_{act,2})\cdot\mathbf{p}_+\cdot\begin{pmatrix} w_1 \\ w_2 \end{pmatrix} e^{-\lambda_+ t}+(k_{act,1},k_{act,2})\cdot\mathbf{p}_-\cdot\begin{pmatrix} w_1 \\ w_2 \end{pmatrix} e^{-\lambda_- t}. \tag{11}$$

It is easy to verify, that the distribution is in fact normalized

$$\int_0^\infty p_w(t)dt=1, \tag{12}$$

and that it has the mean value

$$\langle t\rangle=\frac{k_{12}+k_{21}}{k_{act,1}k_{21}+k_{act,2}k_{12}}. \tag{13}$$

This results in an average reaction rate

$$K\equiv\frac{1}{\langle t\rangle}=\frac{k_{21}}{k_{12}+k_{21}}k_{act,1}+\frac{k_{12}}{k_{12}+k_{21}}k_{act,2}, \tag{14}$$

as a weighted average of the rates in the individual states, with the probabilities of being in these states as weights.

When comparing to experimental data, it is useful to write the waiting time distribution in terms of three parameters, $\lambda_{\pm}$ and ν:

$$p_w(t) = \frac{1+\nu}{2}\lambda_+ e^{-\lambda_+ t} + \frac{1-\nu}{2}\lambda_- e^{-\lambda_- t}. \tag{15}$$

Since the theoretical model has four parameters, a comparison to an experimental waiting time distribution cannot resolve all four parameters.

As an example, let us take the data from TLL, discussed in the main paper. It consist of a series of 7194 consecutive reaction times. In the following figure is shown a (normalized) histogram of the data, including the best fit to theoretical waiting time distribution.

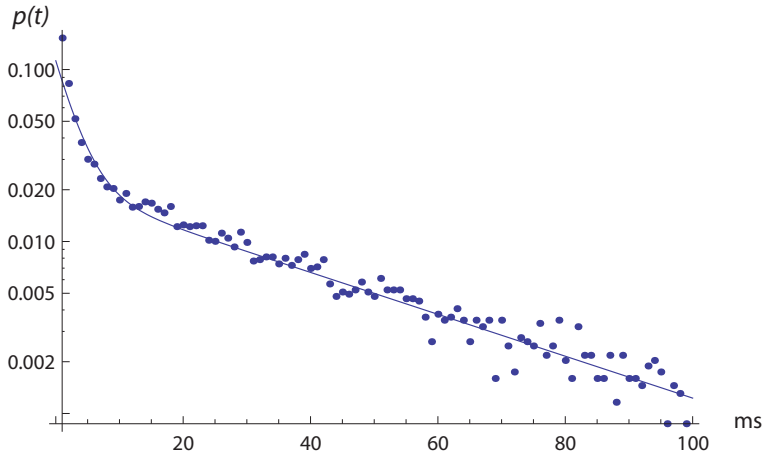

Figure S13. Log-lin-plot of waiting time distribution

The best parameter values are $\lambda_+ = 0.3337$ ms^{-1}, $\lambda_- = 0.0280$ ms^{-1} and $\nu = -0.448$. The theoretical relation between ν and K is

$$\frac{1}{K} = \frac{1+\nu}{2\lambda_+} + \frac{1-\nu}{2\lambda_-}. \tag{16}$$

With the fitting parameters we get $K = 0.0375$ ms^{-1}, consistent with a straightforward calculation of the average value of the experimental waiting times gives $K = \langle t \rangle^{-1}$ ms^{-1} $= 0.03765$ ms^{-1}.

The individual waiting times measured for TLL is accurately described by a double exponential distribution.

A. Waiting time autocorrelations

The model have four parameters, while only three are extracted from the waiting time distribution. The data, however, contain important information in the correlations of subsequent waiting times. In this section we shall discuss such correlations in the model, and extract the missing information to determine all four parameters of the model.

Consecutive waiting times are not necessarily independent. The joint probability density of having n consecutive waiting times $(\tau_1,\ldots,\tau_n)$ is given by

$$p(\tau_1,\ldots,\tau_n)\Delta t_1\cdots\Delta t_n = P(R_{t_n\Delta t_n}\cdots R_{t_1\Delta t_1}|R_{0\Delta t}I), \tag{17}$$

where $\tau_i = t_i - t_{i-1}$. Using the rules of probability theory we can rewrite this $p(\tau_1,\ldots,\tau_n)$ as follows:

$$p(\tau_1,\ldots,\tau_n) = \sum_{i_0,\ldots,i_n} k_{i_n} p_{i_n i_{n-1}}(\tau_n)\cdots k_{i_1} p_{i_1 i_0}(\tau_1) w_{i_0}. \tag{18}$$

The correlation function we are interested in is

$$C_n = \frac{\langle\tau_n\tau_1\rangle - \langle\tau_1\rangle^2}{\langle\tau_1^2\rangle - \langle\tau_1\rangle^2}. \tag{19}$$

This takes values between -1 and 1. If the waiting times τ_n and τ_1 are totally correlated, e.g. if they are proportional, then $C_n = \pm 1$. If the two times are totally uncorrelated, then C_n is 0. The important ingredient in C_n is

$$\langle\tau_n\tau_1\rangle = \int_0^\infty d\tau_1\cdots\int_0^\infty d\tau_n p(\tau_1,\ldots,\tau_n)\tau_n\tau_1 \tag{20}$$

can be rewritten using (8) and the definitions

$$\mathbf{k} = \begin{pmatrix} k_{act,1} & 0 \\ 0 & k_{act,2} \end{pmatrix}, \qquad \mathbf{p}_I = \mathbf{p}_+/\lambda_+ + \mathbf{p}_-/\lambda_-, \qquad \mathbf{p}_M = \mathbf{p}_+/\lambda_+^2 + \mathbf{p}_-/\lambda_-^2 \tag{21}$$

as

$$\langle\tau_n\tau_1\rangle = (k_{act,1}, k_{act,2})\cdot\mathbf{p}_M\cdot\underbrace{\mathbf{k}\cdot\mathbf{p}_I\cdots\mathbf{k}\cdot\mathbf{p}_I}\cdot\mathbf{k}\cdot\mathbf{p}_M\cdot\begin{pmatrix} w_1 \\ w_2 \end{pmatrix}. \tag{22}$$

In this formula there are $n-1$ factors $\mathbf{k}\cdot\mathbf{p}_I$. The eigenvalues of $\mathbf{k}\cdot\mathbf{p}_I$ are 1 and $(1+k_{12}/k_{act,1}+k_{21}/k_{act,2})^{-1}$. The contribution to $\langle\tau_n\tau_1\rangle$ from the eigenvalue 1 will be subtracted in (19), and the correlation function will decay as

$$C_n = \frac{C_2}{\left(1+\frac{k_{12}}{k_{act,1}}+\frac{k_{21}}{k_{act,2}}\right)^{n-2}}. \tag{23}$$

The value of C_2 is a rather complicated function of the model parameters, but can be easily calculated numerically from the general formulas (19) and (22). If one of the states is totally inactive (e.g. $k_{act,2} = 0$), then C_n will be zero, i.e. there are no correlations between consecutive waiting times. This makes sense, because the system in this case always will be in state A_1 immediately after a reaction has taken place, no matter what has happened earlier.

The denominator of (19) is the variance of the waiting time distribution. It can be calculated from

$$\langle \tau_1^2 \rangle = 2(k_{act,1}, k_{act,2}) \cdot \left(\mathbf{p}_+ / \lambda_+^3 + \mathbf{p}_- / \lambda_-^3 \right) \cdot \begin{pmatrix} w_1 \\ w_2 \end{pmatrix}. \tag{24}$$

We shall use these formulas to analyze the TLL data. As mentioned, the waiting time distribution itself can determine three out of the model's four parameters. We shall use the parameter $\eta = \sqrt{k_{12} k_{21}}$ as the fourth parameter, since it measures the strength of the coupling between the two states A_1 and A_2. We expect a large correlation if η is small, since if there are only rare switches between the two states, then a number of consecutive reactions will take place in the same state, hence these reactions will be correlated. In the following figure we have plotted the experimental C_n in a log-lin plot. If the model is correct, this should be a straight line. In red, we show the best fit, which will supply us with a value for the missing parameter, η.

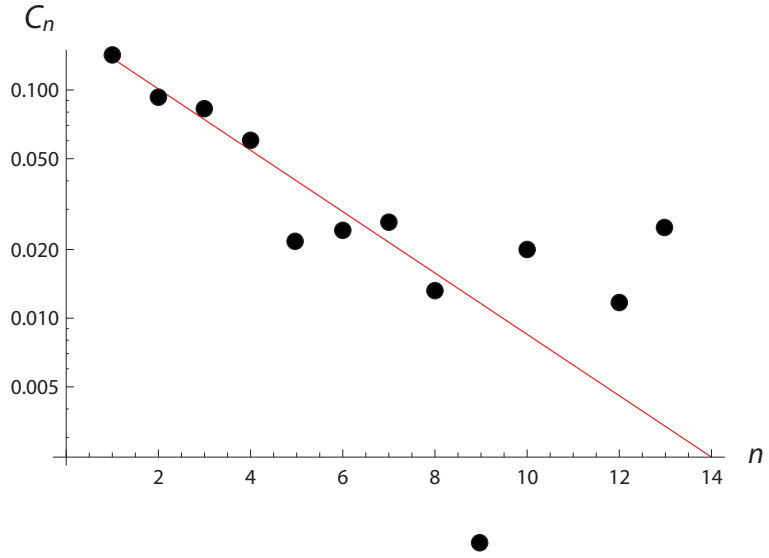

Figure S14. Log-lin plot of the waiting time correlation function C_n.

The best value of η is 0.014 ms^{-1}.

With this value of η, and the three parameters of the waiting time distribution, we can finally obtain the best values of the model parameters. They are (all in ms^{-1}):

$$\begin{array}{ll} k_{act,1} = 0.2700 & k_{12} = 0.0631 \\ k_{act,2} = 0.0254 & k_{21} = 0.0033 \end{array} \tag{25}$$

B. Intensity fluctuations

Intensity fluctuates. The detected intensity consist of two components, the background intensity, $I_b(t)$ and the intensity of photons originating from the system, $I_s(t)$. These two signals are presumably uncorrelated, so the correlation function of the total intensity, $I(t) = I_s(t) + I_b(t)$ can be written

$$\langle I(t+\tau)I(t)\rangle = \langle I_s(t+\tau)I_s(t)\rangle + \langle I_b(t+\tau)I_b(t)\rangle + 2\langle I_s(t)\rangle\langle I_b(t)\rangle. \tag{26}$$

If we subtract the square of the average intensity, $\langle I(t)\rangle^2 = \langle I_s(t)\rangle^2 + \langle I_b(t)\rangle^2 + 2\langle I_s(t)\rangle\langle I_b(t)\rangle$ we get

$$C_I(\tau) = C_s(\tau) + C_b(\tau), \tag{27}$$

where $C_i(\tau) = \langle I_i(t+\tau)I_i(t)\rangle - \langle I_i(t)\rangle^2 = \langle \Delta I_i(t+\tau)\Delta I_i(t)\rangle$, with $\Delta I_i(t) = I_i(t) - \langle I_i(t)\rangle$ being the deviation of the signal from it's average.

So, the intensity correlation function is a simple sum of two contributions, one from the system and one from the background. To the extent that they decay with very different decay times we can easily separate the two signals. This is in contrast to the waiting times, where the background signal can interfere with the waiting times for the system. E.g. a long waiting time in the system can be cut into two shorter waiting times by an accidental burst of photons in the background. The behavior of the intensity correlations can thus be an independent check of the applied thresholding, as well as of the conclusions drawn from the study of waiting times.

We can in fact calculate the intensity correlations for the two state model considered here. A short (duration around 1 ms) burst of photons is associated with each reaction, hence the system intensity can be written

$$I_s(t) = N_0 \sum_i \delta(t - t_i). \tag{28}$$

Here N_0 is the number of photons in each burst. For simplicity we shall assume that this is the same for each reaction. It is straightforward to generalize the

following discussion to the case where N_0 fluctuates around a mean value. The average value, $\langle I_s(t)\rangle$ is equal to $N_0 K$, where K is given by (14). The correlation function evaluates as follows:

$$\begin{aligned}\langle I_s(t+\tau)I_s(t)\rangle &= N_0^2\sum_{ij}\langle\delta(t-t_i)\delta(t-t_j)\rangle \\ &= N_0^2\langle\sum_j\delta(t-t_j)\sum_i\delta(t-t_i+t_j)\rangle \\ &= N_0^2K\langle\sum_i\delta(t-t_i+t_j)\rangle \qquad (29)\\ &= N_0^2K\sum_n\int d\tau_1\cdots\int d\tau_n\delta(\tau-\tau_1\cdots-\tau_n)p(\tau_1,\ldots,\tau_n).\end{aligned}$$

Here $\tau_1,\ldots,\tau_n$ are n subsequent waiting times (in between two bursts at t_i and t_j). This expression is best worked out using a Laplace transform, and the explicit form of $p(\tau_1,\ldots,\tau_n)$ from (18). After a lengthy but straightforward calculation, one arrives at

$$\langle I_s(t+\tau)I_s(t)\rangle = N_0^2K^2\left(1+\frac{k_{12}k_{21}(k_{act,1}-k_{act,2})^2}{(k_{act,1}k_{21}+k_{act,2}k_{12})^2}e^{-(k_{12}+k_{21})\tau}\right). \qquad (30)$$

From this we get the final result:

$$C_s(\tau) = \langle I_s(t)\rangle^2\frac{k_{12}k_{21}(k_{act,1}-k_{act,2})^2}{(k_{act,1}k_{21}+k_{act,2}k_{12})^2}e^{-(k_{12}+k_{21})\tau} \qquad (31)$$

The intensity correlation, $C_s(\tau)$, is thus a single exponential decay with decay constant $k_{12}+k_{21}$.

In the following figure we plot the experimental $C_I(\tau)$ in a log-lin plot.

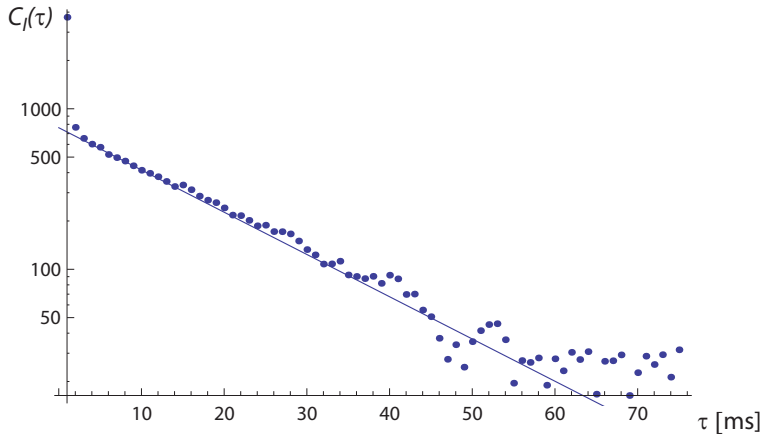

Figure S15. Log-lin plot of the intensity correlation function $C_I(\tau)$.

We see a very high peak with a width of around 2 ms. This we interpret as the contribution to intensity correlation from the background, i.e. $C_b(\tau)$. More interesting is the almost straight line in the experimental plot, which we interpret as the system part of the correlation function, i.e. $C_s(\tau)$. The straight blue line in the plot is the best fit to a single exponential decay, $e^{-\kappa\tau}$. The value for κ is 0.0611 ms^{-1}, which should compared to the expected value $k_{12}+k_{21}$, which we know to be 0.0663 ms^{-1} — a very good agreement. These results thus provide an independent check that correct thresholding has been applied.

C. Activity fluctuations

It is well-known, that activity will fluctuate for a given enzyme. This is also the case for the TLL, studied in this work. In the following figure we plot the running average of the waiting time in a moving time window with a width of roughly 2 second.

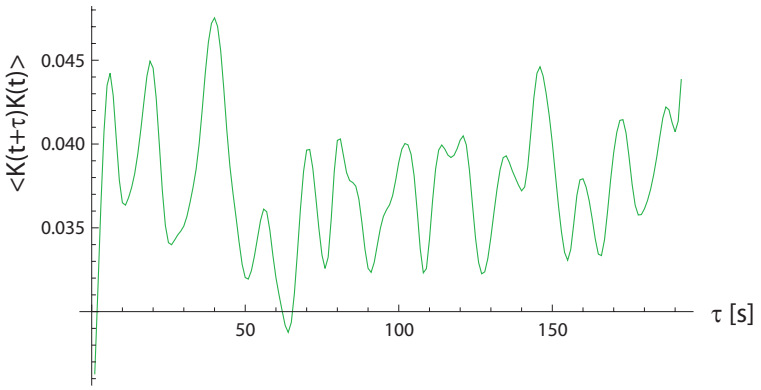

Figure S16. Activity fluctuations. Real data. The function $\langle K(t+\tau)K(t)\rangle$ as a function of τ. $K(t)$ is running average of the intensity. The width, T, of the averaging function is 2 seconds.

It has been suggested, that this would indicate, that the enzyme is moving through different states on a time scale of 5 seconds. This, however, is not a correct interpretation. The activity fluctuations are natural statistical fluctuations of the two-state model, that we are considering in this paper. We have

simulated the model using the parameters found in the previous section. The activity fluctuations of these synthetic data is as follows:

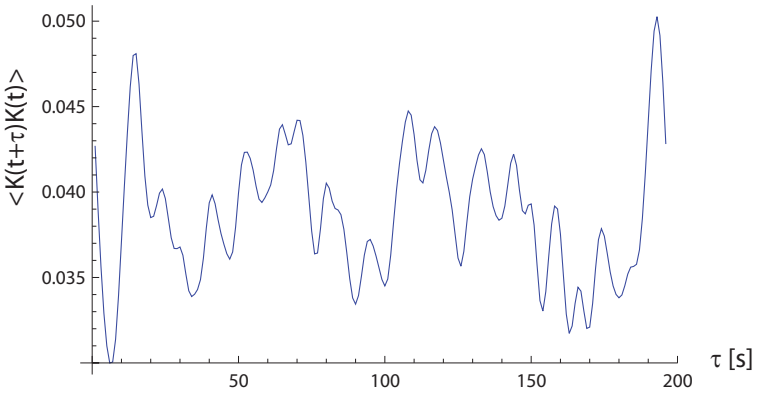

Figure S17. Activity fluctuations. Simulated data. The function $\langle K(t+\tau)K(t)\rangle$ as a function of τ. $K(t)$ is running average of the intensity. The width, T, of the averaging function is 2 seconds.

We see, that the simple two state model also fluctuates on the 10 second scale, and with an amplitude similar to the experimental data. In the final figure we plot the two activity fluctuations in the same graph (green is experiment, blue is model)

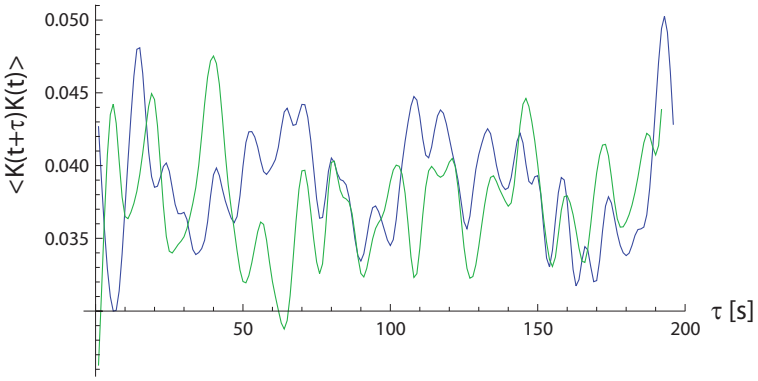

Figure S18. Activity fluctuations. Comparison of real data and simulated data.

Analytically, we can characterize the activity fluctuations by correlations in the time averaged intensity:

$$K(t) = \int f_T(t-t')\Delta I(t')dt'. \tag{32}$$

Here $f_T(t)$ is a function of width, T. It could be the gaussian

$$f_T(t) = \frac{1}{\sqrt{2\pi T^2}} e^{-\frac{t^2}{2T^2}}. \tag{33}$$

The detailed form is not so important. Let us calculate the correlation function of this averaged intensity, $\langle K(t+\tau)K(t)\rangle$. It is related to the intensity correlation function via

$$\langle K(t+\tau)K(t)\rangle = \int\int f_T(t+\tau-t')f_T(t-t'')\langle \Delta I(t')\Delta I(t'')\rangle \, dt' \, dt''. \tag{34}$$

It can be rewritten in terms of the Fourier transforms,

$$\langle K(t+\tau)K(t)\rangle = \int \frac{d\omega}{2\pi} e^{i\omega\tau} |f_T(\omega)|^2 C_I(\omega), \tag{35}$$

where $C_I(\omega)$ is the Fourier transform of the intensity correlation function. If e.g. the intensity correlation function is a single exponential decay: $\langle \delta I(t+\tau)\delta I(t)\rangle = C_0 e^{-\kappa|\tau|}$, then $C_I(\omega)$ becomes

$$C_I(\omega) = C_0 \frac{2\kappa}{\kappa^2+\omega^2}. \tag{36}$$

The Fourier transform, $f_T(\omega)$ of the averaging function, is a function of width $1/T$, as exemplified by the gaussian example, where

$$f_T(\omega) = e^{-\frac{\omega^2 T^2}{2}}. \tag{37}$$

We shall in particular consider the case, where intensity correlations decay faster than the time, T, over which we average. In our example this would correspond to $\kappa T \gg 1$. In the expression (35) the function $|f_T(\omega)|^2$ is thus much more narrow than $C_I(\omega)$, and we can approximate the latter by it's value at $\omega = 0$. Hence we get

$$\begin{aligned} \langle K(t+\tau)K(t)\rangle &\approx C_I(\omega=0)\int \frac{d\omega}{2\pi} e^{i\omega\tau}|f_T(\omega)|^2 \\ &= \frac{C_0}{\sqrt{\pi}\kappa T} e^{-\frac{\tau^2}{4T^2}}. \end{aligned} \tag{38}$$

We see, that this correlation function only depends on the actual intensity through a constant factor C_0/κ. The time dependence is only reflecting the chosen averaging function, and does not reflect actual correlations in the system.

In the opposite limit, where $\kappa T \ll 1$, $C_I(\omega)$ is the narrow function, and we can approximate $|f_T(\omega)|^2$ by it's zero frequency value, i.e. by 1. We then will recover the original intensity correlation function.

We can conclude, that not much is learned by studying the correlation function $\langle K(t+\tau)K(t)\rangle$. All information is already encoded in the direct intensity correlation function $\langle \delta I(t+\tau)\delta I(t)\rangle$.

The two activity states of TLL can be approximated by an active and an inactive one.

In our analysis we developed a statistical model that describes TLL to oscillate between two-activity states with large difference in their inherent activities. (see Figure S19A). Because we found k_{act2} to be on the average ~ 20 time smaller than k_{act1} and independent of bilayer access it can be considered as inactive. Thus TLL may be approximated to oscillated between an active and inactive activity state correlating with the two major enzyme conformational states (see Table S3 and Figure S17B). The main advantage of this simplification is that to adequately describe TLL enzymatic behavior only 3 independent parameters, directly encoded in the waiting time distribution, are employed instead of 4 when using 2 non-zero activity states. To test if this approximation influences the validity of our findings we quantified both the probability of being on the highly active state P_{act} and the inherent activity of that state k_{act1} as a function of PEG concentrations using the model with 2 non-zero activity states. As shown in Figure S19 we found qualitatively identical results independent of the presence of one or two activity states (see Table S3). Systematic restriction of enzymes from accessing the effector-bilayer in both cases does not significantly influence the enzymes inherent activity but primarily confers a shift in the equilibrium towards the highly active states. Therefore to simplify statistical analysis and minimize error we chose to approximate TLL behavior to oscillate between an active and an inactive state. The individual kinetics rates for all single molecules studied as shown in Figure S20.

The rest of the enzymes examined in this contribution have not been reported to undergo to an inactive conformational state to the best of our knowledge. Because therefore there is no direct correlation between conformational and activity states we used the more generic model with 2 activity states to describe their kinetic behavior. All enzymes tested where found to oscillate between two activity states with markedly different inherent activities rather than a continuous distribution of them.

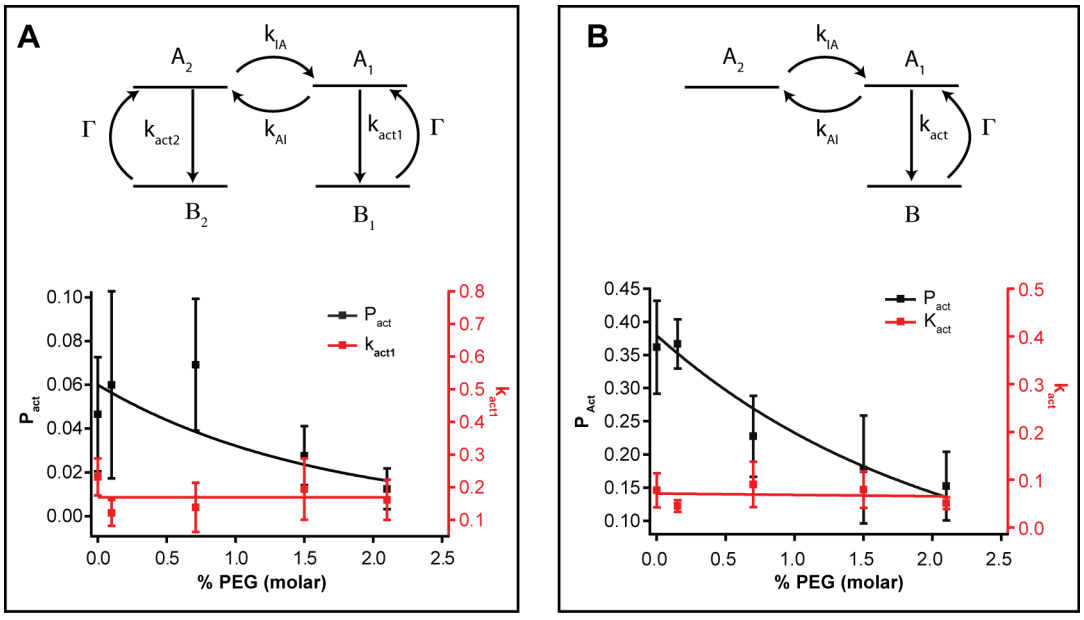

Figure S19. Probability of TLL to reside on the highly active state as a function of bilayer accessibility calculated by using a model with a single active state **A** or two active states **B**. Independently of the

model qualitatively identical results are obtained. Systematically restricting enzymes from accessing the effector-bilayer confers a shift in the equilibrium towards the highly active states. Data are fitted with single exponential decays and error bars correspond to s.d. between values of different single enzymes.

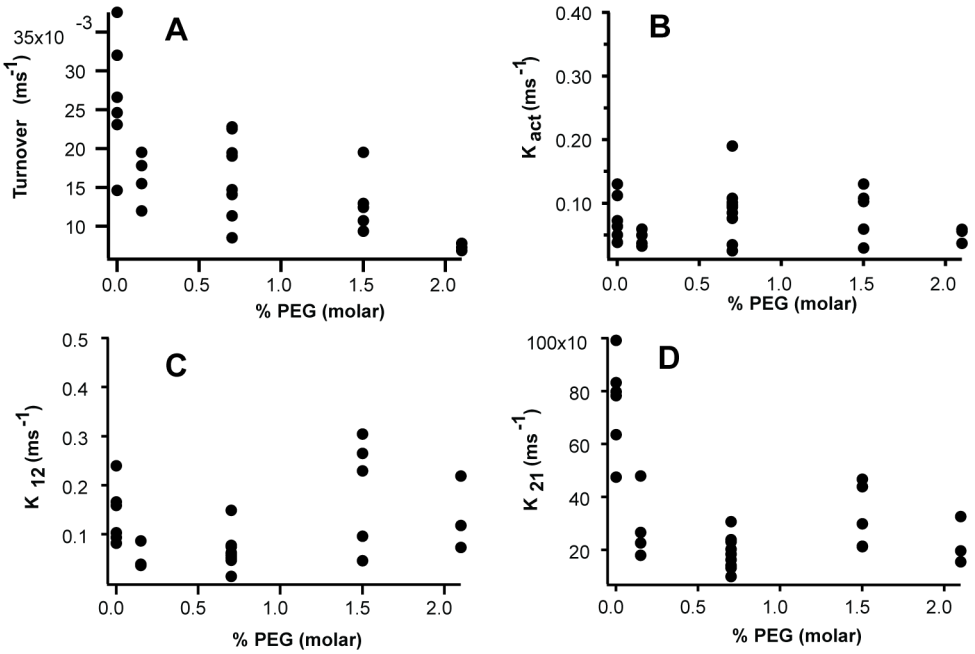

Figure S20. Kinetic rates of all single molecule as a function of PEG concentration. **A.** Average activity rate of the individual TLL molecules **B.** k_{act} of each TLL molecule. **C.** k_{12} and **D.** k_{21} of individual TLL molecules.

Bayesian comparison of two activity states model with multiple activity states models.

To compare the 2 activity state model with continuous multistate model we will employ the Bayes theorem.

$$\frac{P(u_1/N_i)}{P(u_2/N_i)} = \frac{P(N_i/u_1)}{P(N_i/u_2)} \cdot \frac{P(u_1)}{P(u_2)} \quad \textbf{(39)}$$

The two activity state (model 1) is described:

$$f(t,\gamma,\lambda_+,\lambda_-) = kactPact(t) = \frac{1-\gamma}{2}\lambda_+ \exp(-t\lambda_+) + \frac{1+\gamma}{2}\lambda_- \exp(-t\lambda_-) \quad \textbf{(40)}$$

A typical model with a distribution of activities (model 2) is described by

$$\Phi_{off}(t) = \Phi_0 e^{-(t/\tau)^a} \quad \textbf{(41)}$$

where

$$\Phi_0 = \frac{1}{\int_0^\infty e^{-(1/\tau)^a} dt} = \frac{\alpha/\tau}{\Gamma(1/\alpha)} \quad \textbf{(42)}$$

We binned at 1ms, from 1 to 100, we have Ni waiting time locate in i^{th} bin (i=1…100), when the total number of waiting time is N. Each model has a certain probability P in i^{th} bin. The predicted number of waiting time in model 1 is $u_1 = P_1 \times N$ and in model 2 is $u_2 = P_2 \times N$.

But in experiment, the real number of waiting time is N_i

Comparing the two models using Bayes theorem consists of two factors:

the ratio $\frac{P(u1)}{P(u2)}$ showing the likelihood of each model to be correct. We will consider that as 1, and

the ratio of probabilities $\frac{P(u_1/N_i)}{P(u_2/N_i)}$ of having u_1 waiting time in this bin according to model 1 for N_i experimental data / Probability of have u_2 waiting time according to model 2 for N_i experimental data.

These probabilities are given by Poisson distributions

$$P(N_i/u_1) = \frac{u_{1i}^{N_i}}{N_i} e^{-u_{1i}} \quad \textbf{(43)} \quad \text{and}$$

$$P(N_i/u_2) = \frac{u_{2i}^{N_i}}{N_i} e^{-u_{2i}} \quad \textbf{(44)}$$

$$\text{Since } P(D/M1) = \prod_{i=1}^{N} P(N_i/u_{1i}) = \prod_{i=1}^{N} \frac{u_{1i}^{N_i}}{N_i} e^{-u_{1i}} \quad \textbf{(45)}$$

The ratio (eq 39) becomes

$$\frac{P(u_1/N_i)}{P(u_2/N_i)} = \frac{P(N_i/u_1)}{P(N_i/u_2)} \cdot \frac{P(u_1)}{P(u_2)} = \frac{\prod_{i=1}^{N} \frac{u_{1i}^{N_i}}{N_i} e^{-u_{1i}}}{\prod_{i=1}^{N} \frac{u_{2i}^{N_i}}{N_i} e^{-u_{2i}}} \quad \textbf{(46)}$$

For the data in Figure S23A we found $\frac{P(u_1/N_i)}{P(u_2/N_i)} = 2.34 \times 10^{34}$ showing that a double exponential fits the waiting time distribution significantly better than stretched exponential.

<u>Probability of a vesicle anchored TLL to reach the PEGylated bilayer</u>

In Figure 3 we showed the overall TLL activity to decrease exponentially depending on the PEG density on liposomes. If the overall activity (A_{TLL}) is dependent on the accessibility to the liposomes it should be proportional to the enzyme's residence probability on the PEGylated bilayer. This residence probability (P_r) is dependent on the surface pressure (Π_p) and the cross sectional area of TLL (A_{pro}) and is given by:

$$A_{TLL} = kP_r = kP_0 \exp\left(\frac{-A_{pro}\Pi_p}{k_B T}\right) = A_0 \exp\left(\frac{-A_{pro}\Pi_p}{k_B T}\right) \quad \textbf{(47)}$$

where $\Pi_p = \frac{f_{PEG} k_B T}{A_L}$, [14]: **(48)**

f_{PEG} is the membrane molar fraction of PEG, A_L is the cross section of lipid and A_{pro} is the cross section area of TLL given by $A_{pro} = \pi r^2$. A_0 is the activity of TLL without steric hindrance thus absorbing the proportionality constant k and the residence probability P_0 at 0 % PEG.

Combining **47** and **48** we obtain the following

$$A_{TLL} = A_0 \exp\left(\frac{-A_{pro} f_{PEG}}{A_L}\right) \quad \textbf{(49)}$$

Applying a exponential fit to the data of Figure 3C we obtain a exponential constant A_0=22 ± 3 s^{-1} and a surface ratio of $\frac{A_{pro}}{A_L}$=49.2 ± 9 s^{-1} which is consistent with a surface ratio of 40.6 calculated from A_L = 0.65 nm and A_{pro}=π (2.9 nm)^2 found in the literature [15], thus supporting our approximation that the reduced enzymatic activity is due to the restricted access to the bilayer.

The fact that the data of Figure 3D with eq49 resulted in C = 0.32 ± 0.02 and A_{pro}/A_L = 48.1 ± 16 also in agreement with the calculated surface ratio of 40.6 strongly supports that regulatory interactions primarily redistribute TLL's probability to reside in the highly active state.

Note that CFDA is not TLL's natural substrate. We obtained however comparable trends of activity increase upon regulatory interaction with bilayers as observed for natural substrates albeit with smaller amplitudes.

Mechanistic origin of TLL activity regulation

Shifting an equilibrium towards the active state in a two activity state model could originate by: a) stabilization of the active state, b) destabilization of the inactive state or c) a combination of both. Because we are measuring the conversion rate from the inactive to the active state (k_{21}) as well as the reverse rate back to the inactive state (k_{12}), we can calculate the energy barriers between the two states.

To draw the energy landscape of lipase upon regulation a reference point is needed that is not dependent on effector concentration. Our findings support that the active state of lipase corresponds to the open lid conformation obtained when the enzyme resides on liposomes while when the enzyme is displaced from the bilayer it undergoes to inactive state. Because the inactive state corresponds to enzyme residing away from the effector bilayer, we will assume it to be independent of membrane modification by PEG. Therefore the energy level of the inactive state is taken as constant independently of bilayer access and is used as reference point to draw the energy landscape. Lipase regulation then originates from energetic stabilization of the active state and shift of the population equilibrium to the active conformations.

To dissect the origin of the population shift we plotted the average exchange rate constants for the lipase as a function of bilayer access (see Figure S21). In spite the large scattering of the data, due to static disorder between different enzymes, we recorded k_{12} values that are not dependent on bilayer access in Figure S21A. We found k_{21} on the other hands to be reduced by 4 fold as bilayer access is restricted. Based on this we conclude that regulation of lipase proceeds via equal

energetic stabilization of the active state and the transition state to the active state (regulatory coordinate of Figure 4).

As shown in Figure S21, regulation of enzyme activity may originate from i) shift in the average distribution of multiple activities (grey arrow), ii) redistribution of a two activity state equilibrium towards the highly active state (green arrow), iii) induction of new activity state (blue arrow). Our findings provide for the first time concrete validation that an enzyme other than ion-channels function in accordance to the hypothesis that regulatory interactions do not create new states of different inherent activity but primarily redistribute the conformational equilibrium towards one of the preexisting states.

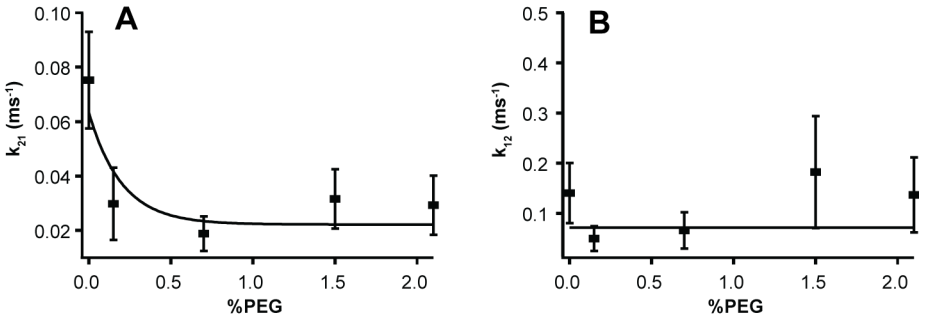

Figure S21. Interconversion rates of equilibrium between the 2 activity states of TLL as a function of PEG concentration. **A.** The inactive to active transition k_{21} is strongly dependent on the presence of effector bilayer. Increasing enzyme accessibility confers a ~ 4 fold increase in the transition rate above the noise. **B.** The active to inactive transition k_{12} shows within noise no significant dependence on bilayer accessibility. Thus regulation appears to occur via stabilization of the active state and the transition state. Error bars correspond to standard deviation of values for individual enzymes.

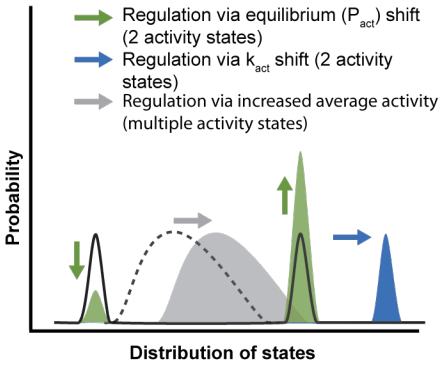

Figure S22. Regulation of enzyme activity may occur via i) shift in the average distribution of multiple activities (grey arrow), ii) redistribution of a two activity state equilibrium towards the highly active state (green arrow), iii) induction of new activity state (blue arrow). Our findings support the presence of two activity states over a continuous distribution of them. Regulatory interactions do not introduce a new activity state but simply shift the equilibrium towards the highly active states.

Oscillation between a discrete number of activity states describes the behavior of additional monomeric enzymes.

In Figure S23A we plotted the entire histogram of TLL waiting time distribution showing that a double exponential decay prevalently describes the data of TLL as compared to a stretched exponential decay. Taken together with the data of Figures S13-18 we concluded that TLL toggles between two activity states instead of a continuous distribution of them.

Next we reevaluated whether other monomeric enzymes possess a discrete number of states.

We recorded the activity trajectory of Lipase from *Candida Antarctica* (*CALB*) [16] as a representative hydrolytic enzyme. *CALB* was chosen because it does not possess a lid and therefore its activity is not regulated by bilayer accessibility (see Figures S1-10). A single cyst variant of the enzyme, ensuring monodirectional coupling, was conjugated to SAV^{488} added on liposome and its activity was monitored at saturating CFDA concentrations (see Figures S1-10 for controls). As shown in Figure S23B fitting of the waiting time distribution of CALB with double exponential decay resulted in significantly improved fitting as compared to a stretched exponential decay (see Figure S23B inset). Additionally the waiting time autocorrelation function was found to follow a monoexponential decay consistent with the two activity states model (see Figure S24A). We found CALB to interconvert between two activity states with activities k_{act1} = 0.218 ms^{-1} and k_{act2} = 0.012 ms^{-1} and interconversion rates k_{12} = 0.08 ms^{-1} and k_{21} = 0.011 ms^{-1} (See Table S2). Furthermore the intensity autocorrelation $C_I(t)$ can be described with monoexponential decay (see Figure S25A) further justifying our two activity state approximation. Despite the small deviation in long time scales the $C_I(t)$ decays with an exponent $K_{(I)}$ =0.09 ms^{-1} that matches the sum of the two interconversion rates $k_{12} + k_{21}$= 0.08 + 0.011 = 0.091 as proposed for two activity states models[17,18]. In full agreement with TLL data CALB appears to oscillate between two activity states with considerably different inherent activities rather than a continuous distribution of them.

To further examine of additional enzyme besides lipases adopt analogous catalytic behavior we obtained the published activity trace of Nitrite Reductase from *Alcaligenes faecalis* as a representative of redox enzymes. Data recorded at saturating conditions (500 μM nitrite) were provided by professor G.W. Canters [19]. As shown in Figure S23C fitting of the waiting time distribution of Nitrite reductase with double exponential decay resulted in significantly improved fitting as compared to a stretched exponential decay. In agreement with the two activity state approximation the waiting time autocorrelation decays monoexponetially (see Figure S24B). Calculation of the reaction rates resulted in k_{act1} = 0.022 ms^{-1} and k_{act2} = 0.004 ms^{-1} and interconversion rates k_{12} = 0.022 ms^{-1} and k_{21} = 0.011 ms^{-1} (See Table S2). Furthermore the intensity autocorrelation $C_I(t)$ can be described with monoexponential decay further justifying our two activity state approximation (see Figure S25B). Despite the small deviation in long time scales the $C_I(t)$ decays with an exponent $K_{(I)}$ =0.03 ms^{-1} that matches the sum of the interconversion rates $k_{12} + k_{21}$= 0.022 + 0.011 = 0.033 ms^{1} as proposed for two activity states models [17,18]. We conclude therefore that Nitrite reductase also oscillates between two activity states with considerably different inherent activities rather than a continuous distribution of them.

However, in agreement with previous findings [20,21], β-galactosidase and chymotrypsin could not be fitted with a two-state model (see Figure S26). This might be expected for β-galactosidase, which is composed of four monomers that could catalyze independently of each other, but suggests chymotrypsin has indeed more than two states.

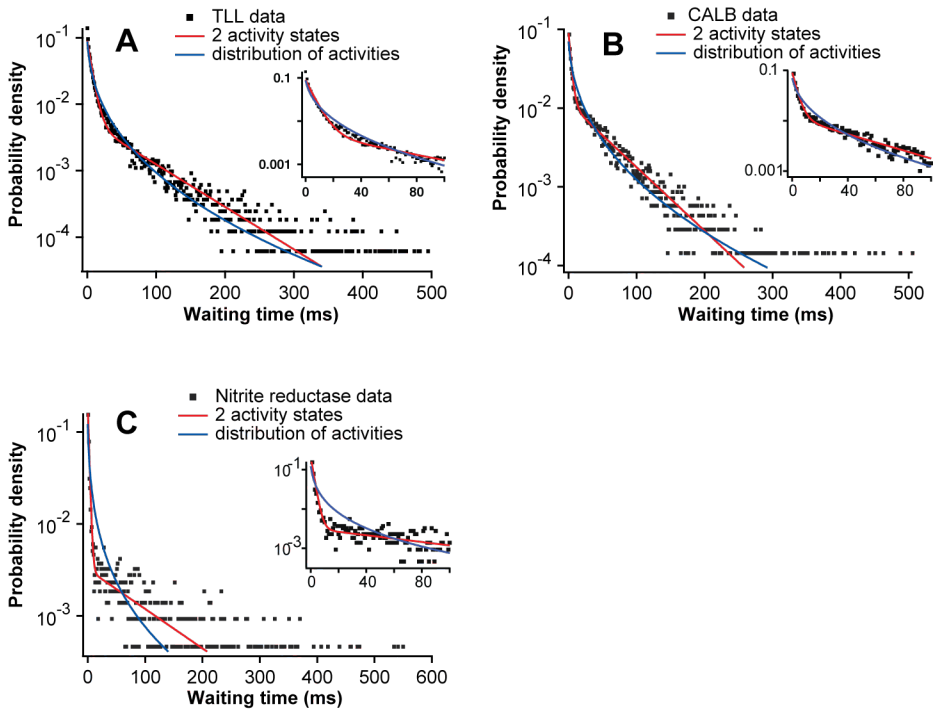

Figure S23. Full waiting time distribution and their fits for the enzyme studied. Data are fit with a double exponential decay from the 2 activity states model (blue line) and the stretched exponential (red line) of a multistate model with continuous activity, for **A**. TLL **B**. CALB **C**. Nitrite reductase from *Faecalis Alcaligenis* **A.** CALB data are obtained at saturating CFDA concentrations of 100 μM **B.** TLL data are at saturating CFDA concentrations of 100 μM, **C.** Nitrite reductase data are obtained at saturating 500 μM nitrite concentration [19] In all cases a significantly better fitting is obtained with the 2 activity states model (double exponential) as compared to a model with a continuous distribution of activities (stretched exponential)

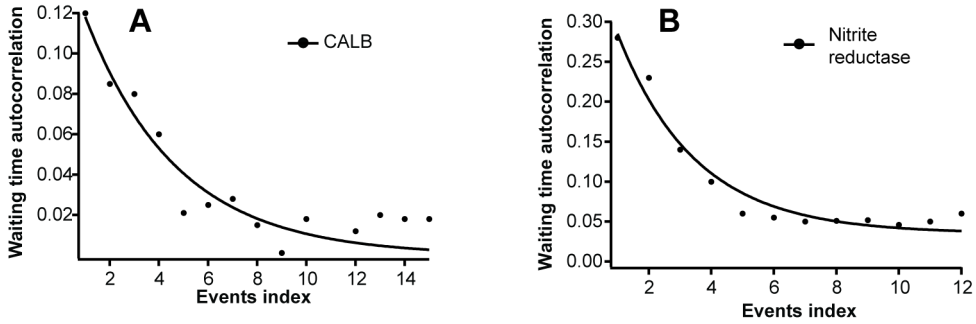

Figure S24. A. Waiting time autocorrelations for **A.** CALB and **B.** Nitrite reductase. Data are fit in both cases with single exponentials verifying that two activity states accurately describe the activity behavior of these enzymes.

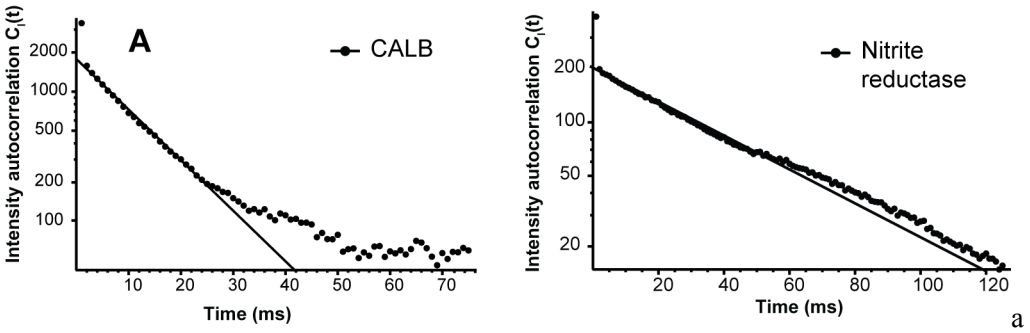

Figure S25. A. Intensity autocorrelations for **A.** CALB and **B.** Nitrite reductase fitted in both cases with single exponentials. **A.** CALB intensity autocorrelation $C_I(t)$ can be described with monoexponetially decay in agreement with our two activity state approximation. $C_I(t)$ decays with an exponent $K_{(I)}$ =0.09 ms^{-1} in full accordance with the sum of the two interconversion rates $k_{12} + k_{21}$= 0.08 + 0.011 = 0.091. **B.** Despite the small deviation in long time scales, that deserves more investigation, $C_I(t)$ of Nitrite reductase decays with an exponent $K_{(I)}$ =0.03 ms^{-1} that matches the sum of the interconversion rates $k_{12} + k_{21}$= 0.022 + 0.011 = 0.033 ms^{1}

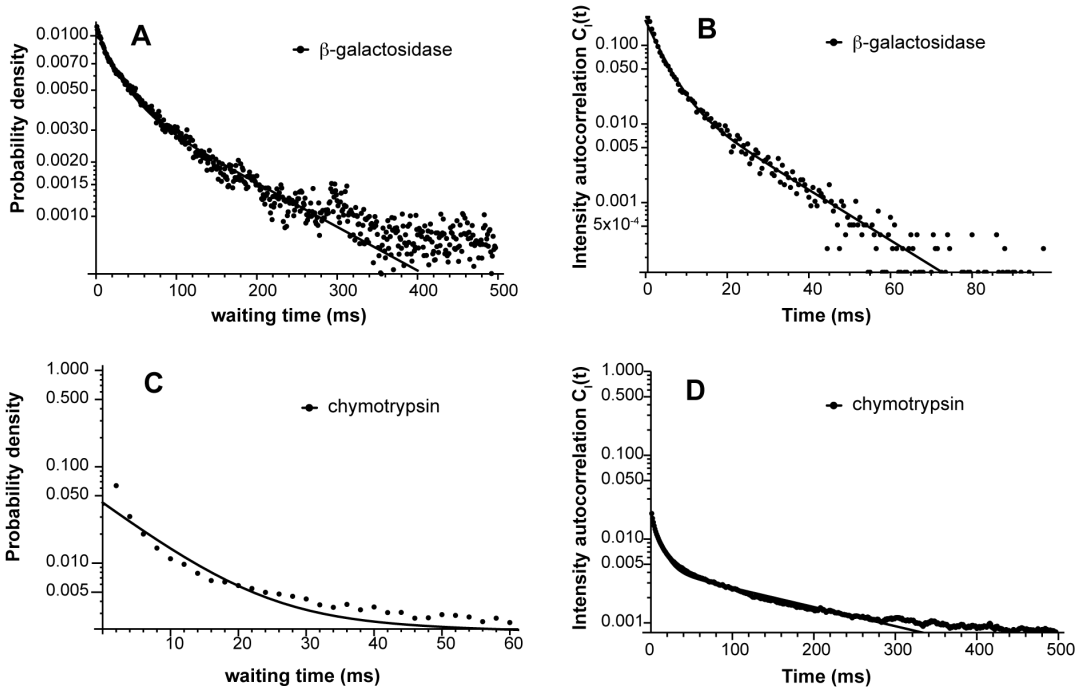

Figure S26. Waiting time distribution and intensity autocorrelation for **A. B.** β-galactosidase and **C. D.** chymotrypsin respectively showing them to exhibit more than two activity states. **A**. The waiting time distribution of β-galactosidase can be fitted with a double exponential decay. **B.** The intensity autocorrelation cannot be accurately fitted with single exponential indicating that the tetrameric β-galactosidase exhibits more that two activity states, in agreement with earlier findings [20]. Data are fit with double exponential to guide the eye. **C.** Zoomed in region of the waiting time distribution of chymotryspin. A double exponential decay does not accurately fit the data. **D.** The intensity autocorrelation does not decay monoexponentially suggesting chymotrypsin to exhibit more than two activity states. Data are fitted with double exponential decay to guide the eye.

Table S1. Calculated values of K_{act} and P_{act} for TLL for various PEG concentrations

PEG concentration (M)	k_{act}	P_{act}	k_{12}	k_{21}	**Number of enzymes**
0%	0.08 ± 0.04*	0.36 ± 0.07	0.14 ± 0.06	0.075 ± 0.02	6
0.15	0.05 ± 0.01	0.37 ± 0.04	0.05 ± 0.03	0.029 ± 0.02	4
0.7	0.09 ± 0.04	0.23 ± 0.06	0.07 ± 0.04	0.019 ± 0.06	9
1.5	0.08 ± 0.04	0.18 ± 0.08	0.19 ± 0.11	0.032 ± 0.01	5
2.1	0.05 ± 0.01	0.15 ± 0.05	0.14 ± 0.07	0.029 ± 0.01	4

*Error bars correspond to standard deviations between values of different single enzymes.

Table S2. Inherent activity rates and interconversion between the two activity states of rates for TLL. CALB and Nitrite reductase using 4 state model.

Enzyme	k_{act1}	k_{act2}	k_{12}	k_{21}
TLL (0%PEG)*	0.24 ± 0.05[#]	0.017 ± 0.005	0.054 ± 0.03	0.0025 ± 0.002
CALB	0.218	0.012	0.08	0.011
Nitrite reductase	0.022	0.004	0.022	0.011

* Average valued of 5 individual enzymes

[#] Error bars correspond to standard deviations between values of different single enzymes

Table S3. Calculated ratio of K_{act2} / K_{act2} for TLL for various PEG concentrations

PEG concentration (M)	k_{act2} / k_{act2}	**Number of enzymes**
0%	14.1 ± 4.6*	6
0.15	9.4 ± 3.4	4
0.7	19.3 ± 10.6	9
1.5	25.2 ± 12.1	5
2.1	24.7 ± 11.9	4

*Error bars correspond to standard deviations between values of different single enzymes

References

(1) Kunding, A. H.; Mortensen, M. W.; Christensen, S. M.; Stamou, D. *Biophys J* **2008**, *95*, 1176.

(2) Christensen, S. M.; Bolinger, P.-Y.; Hatzakis, N. S.; Mortensen, M. W.; Stamou, D. *Nature Nanotechnology* **2011**, *7*, 51.

(3) Hatzakis, N. S.; Bhatia, V. K.; Larsen, J.; Madsen, K. L.; Bolinger, P. Y.; Kunding, A. H.; Castillo, J.; Gether, U.; Hedegard, P.; Stamou, D. *Nat. Chem. Biol.* **2009**, *5*, 835.

(4) Svendsen, A.; Clausen, I. G.; Patkar, S. A.; Borch, K.; Thellersen, M. In *Lipases, Part A* 1997; Vol. 284, p 317.

(5) Skjot, M.; De Maria, L.; Chatterjee, R.; Svendsen, A.; Patkar, S. A.; Ostergaard, P. R.; Brask, J. *Chembiochem* **2009**, *10*, 520.

(6) Blank, K.; Morfill, J.; Gumpp, H.; Gaub, H. E. *J. Biotechnol.* **2006**, *125*, 474.

(7) Petrasek, Z.; Schwille, P. *Biophys. J.* **2008**, *94*, 1437.

(8) Lakowicz, J. R. *Principles of Fluorescence Spectroscopy*; Kluwer Academic/Phenum Publisher, 1999.

(9) Dukes, K. D.; Rodenberg, C. F.; Lammi, R. K. *Anal. Biochem.* **2008**, *382*, 29.

(10) Israelachvili, J. *Proc. Natl. Acad. Sci. U. S. A.* **1997**, *94*, 8378.

(11) Peng, Z. G.; Hidajat, K.; Uddin, M. S. *J. Colloid Interface Sci.* **2004**, *271*, 277.

(12) Cajal, Y.; Svendsen, A.; De Bolos, J.; Patkar, S. A.; Alsina, M. A. *Biochimie* **2000**, *82*, 1053.

(13) Cajal, Y.; Svendsen, A.; Girona, V.; Patkar, S. A.; Alsina, M. A. *Biochemistry* **2000**, *39*, 413.

(14) NopplSimson, D. A.; Needham, D. *Biophys. J.* **1996**, *70*, 1391.

(15) Zhu, K.; Jutila, A.; Tuominen, E. K. J.; Kinnunen, P. K. J. *Protein Sci.* **2001**, *10*, 339.

(16) Flomenbom, O.; Velonia, K.; Loos, D.; Masuo, S.; Cotlet, M.; Engelborghs, Y.; Hofkens, J.; Rowan, A. E.; Nolte, R. J. M.; Van der Auweraer, M.; de Schryver, F. C.; Klafter, J. *Proc. Natl. Acad. Sci. U. S. A.* **2005**, *102*, 2368.

(17) Kou, S. C.; Cherayil, B. J.; Min, W.; English, B. P.; Xie, X. S. *J. Phys. Chem. B* **2005**, *109*, 19068.

(18) Yang, S. L.; Cao, J. S. *J. Chem. Phys.* **2002**, *117*, 10996.

(19) Kuznetsova, S.; Zauner, G.; Aartsma, T. J.; Engelkamp, H.; Hatzakis, N.; Rowan, A. E.; Nolte, R. J. M.; Christianen, P. C. M.; Canters, G. W. *Proc. Natl. Acad. Sci. U. S. A.* **2008**, *105*, 3250.

(20) English, B. P.; Min, W.; van Oijen, A. M.; Lee, K. T.; Luo, G. B.; Sun, H. Y.; Cherayil, B. J.; Kou, S. C.; Xie, X. S. *Nat. Chem. Biol.* **2006**, *2*, 87.

(21) De Cremer, G.; Roeffaers, M. B. J.; Baruah, M.; Sliwa, M.; Sels, B. F.; Hofkens, J.; De Vos, D. E. *J. Am. Chem. Soc.* **2007**, *129*, 15458.